Design and Instrument Characterization of the High-Energy Resolution relativistic electron Telescope (HERT) using Geant4 Simulation

by

Skyler Krantz

A thesis submitted to the Graduate Faculty of
Auburn University
in partial fulfillment of the
requirements for the Degree of
Master of Science

Auburn, Alabama
May 6, 2023

Keywords: HERT, Geant4, Space Instrumentation

Approved by

Masatoshi Hirabayshi, Co-Chair, Professor of Aerospace Engineering
Hong Zhao, Co-Chair, Professor of Physics
Davide Guzzetti, Professor of Aerospace Engineering
Michael Fogle, Professor of Physics

Abstract

Earth's outer radiation belt is filled with relativistic and ultrarelativistic electrons in the MeV energy range and above. These highly energetic electrons pose significant threats to avionics and humans in space, and understanding their dynamics has been an urgent need. In the post Van Allen Probes era, measurements of radiation belt populations heavily rely on small space missions such as CubeSats and SmallSats. The Miniaturized High-Energy-Resolution relativistic electron Telescope (HERT) is a compact ($\leq$3U) telescope designed for a CubeSat mission in geosynchronous transfer orbit (GTO). HERT's main objective is to provide high-energy-resolution measurements of outer belt electrons in an energy range of $\sim$1 – 7 MeV to help differentiate various mechanisms that accelerate electrons to relativistic and ultrarelativistic energies. Geant4 simulations were conducted to characterize the instrument responses. A novel method of using a spherical cap particle source in Geant4 simulation was developed for more efficient instrument characterization. Combined with bow tie analysis, it is demonstrated that HERT will have an energy resolution of 5% for $\sim$1.5 – 3 MeV electrons and 10% for $\sim$3-7 MeV. In addition, using the AE9 model, the instrument is shown to have statistically sufficient count rates in the outer belt while not saturating the electronics. With a compact configuration and higher energy resolution in comparison to previous instruments, HERT will significantly contribute to the quantitative understanding of the radiation belt electron dynamics.

Acknowledgments

To the entire HERT team, I am grateful to have worked with you on this project, and thank all of you for your support. I would like to thank my friends, family, and especially my wife Hannah for their encouragement and support during my time at Auburn. Finally, I would like to thank NASA for their support as HERT is supported through NASA grant 80NSSC21K1041.

Table of Contents

List of Figures

List of Tables

Chapter 1

Introduction

Earth's outer radiation belt is filled with high energy electrons and protons provided by solar wind, galactic cosmic rays, and other sources. These energetic particles form a harsh radiation environment surrounding Earth. This space radiation environment can produce both negative short-term effects like increase in ionspheric density [1] and negative long-term effects on spacecraft such as solar panel degradation [2]. It poses significant risk to satellites and astronauts in space, as well as technical systems on the ground [3]. Thus, it is vital to understand the radiation environment and its dynamics around Earth.

One of the long-standing questions about the radiation belts is how electrons are accelerated to relativistic and ultrarelativistic energies. Two acceleration mechanisms have been proposed: inward radial transport [4] and local acceleration [5, 6]. Both of these mechanisms have different characteristics and lead to unique phase space density signatures. Utilizing unprecedented measurements of radiation belt populations by the Van Allen Probes [7], various studies demonstrated the importance of both mechanisms, though their relative importance to electrons with different energies is still under considerable debate. Specifically, for relativistic and ultrarelativistic electrons, it has been shown that the acceleration mechanism is highly energy-dependent [8, 9, 10, 11], and the inward radial transport plays a significant role in accelerating electrons to ultrarelativistic energies in the outer belt up to the Van Allen Probes' apogee($\sim$5.8 RE) [12, 13]. However, due to limited in situ observations, the region between the Van Allen Probes' apogee and GEO is underexplored, despite the fact that the electron concentration changes dramatically in this region [14]. To fully understand the relativistic and ultrarelativistic electron dynamics

and accurately quantify the effect of different acceleration mechanisms, in-situ electron measurements across the entire radiation belt region up to GEO are needed. In the post Van Allen probe era, radiation belt measurements will rely more on smallsat and cubesats missions which provide cost-effective solutions required to improve our understanding of the radiation belt dynamics. Thus, miniaturized instruments that are capable of providing high-quality measurements with low power/mass/volume budget become essential.

On the other hand, one telltale signature of ongoing radial diffusion is the periodic flux oscillations of radiation belt electrons with frequencies near the electron drift frequency [15, 16, 17, 18, 19, 20, 21, 22]. The flux oscillations provide insight into the resonant interaction between the radiation belt particles and ultra-low-frequency (ULF) waves and the radial diffusion processes, allowing a greater understanding of electron belt dynamics. However, due to the energy-dependent drift frequency of radiation belt electrons, to observe these flux oscillations, the instrument must have a high energy resolution [17], but the energy resolution of past and current measurements of $\geq$ MeV electrons (e.g., dE/E $\sim 30\%$ for REPT instruments on the Van Allen Probes [23, 24]) is not sufficient to clearly discern the detailed flux oscillation signature. An instrument that is capable of taking high-energy-resolution measurements of the radiation belt electron core population thus has the potential to greatly advance the understanding and quantification of the radial transport process.

The High Energy Resolution relativistic electron Telescope(HERT) is a miniaturized particle telescope designed for a CubeSat mission in geosynchronous transfer orbit (GTO). HERT follows the heritage from the REPT instrument [23, 24] on the Van Allen Probes and the REPTile instrument [25, 26] on the Colorado Student Space Weather Experiment (CSSWE) [27] to provide high energy resolution electron flux measurements for 1-7 MeV electrons. The main design requirements for HERT are the miniaturization ($\leq$3U) and high energy spectral resolution (dE/E $\leq 12\%$). This energy resolution will provide the capability to observe flux oscillations of radiation belt electron core population across the whole outer radiation belt while the instrument is in GTO. In turn, these observations can help disentangle the two acceleration mechanisms of relativistic and ultrarelativistic electrons in the outer radiation belt and advance our understanding of radiation belt electron dynamics.

This work focuses on the instrument design and instrument performance characterization of HERT. Chapter 2 details the instrument design. Chapter 3 details the Geant4 simulation setup used to characterize instrument performance. Chapter 4 show the instrument performance characterized using Geant4 simulations. Chapter 5 is a discussion on how Geant4 was utilized during the design process. Chapter 6 is the conclusion.

Chapter 2

Instrument Design

A cross-section of the instrument (left panel) and instrument head (right panel) of HERT can be found in Fig. 2.1. Material marked in light grey is aluminum, dark grey is tantalum, orange is Beryllium (Be), pink is Tungsten or Tungsten-epoxy, yellow is silicon detectors, and blue is stainless steel. Following its heritage from REPT and REPTile, HERT is composed of nine solid state silicon detectors in a telescope type configuration. The first detector has a diameter of 20 mm while the other detectors have a diameter of 40 mm. Tungsten sheets with a thickness of 0.5 mm form a 5 mm thick stack providing shielding at the front and back of the detector stack. A 4 mm thick tungsten epoxy chamber comprises the shielding surrounding the detector stack. This shielding limits non-field-of-view (FOV) particles from reaching the detector stack. A tantalum collimator with five knife-edged baffles with openings of 18 mm enforces the desired FOV of approximately 33°. The baffles have a knife edge of 45° and are spaced so that non-FOV particles cannot reach the detector stack without interacting with multiple baffles [28]. Tantalum is used for the collimator as a high Z material (Z=73) that adequately prevents secondary particle generation [25]. A 1.5 mm thick Beryllium window at the end of the collimator acts as a high pass filter and prevents lower energy particles ($\leq$ 0.5 MeV) from reaching the detectors. Stainless steel pins provide alignment during assembly and constrain the detectors from rotating. Finally, an aluminum chassis provides another layer of shielding, but more importantly the structure for instrument housing and mounting for cubesat assembly.

As with previous instruments, HERT estimates the incident energy of electrons by the deposited energy in the detector stack. Due to electronic noise, the detector threshold for each detector is set to 0.1 MeV. Therefore, the electrons must deposit more than this in an individual

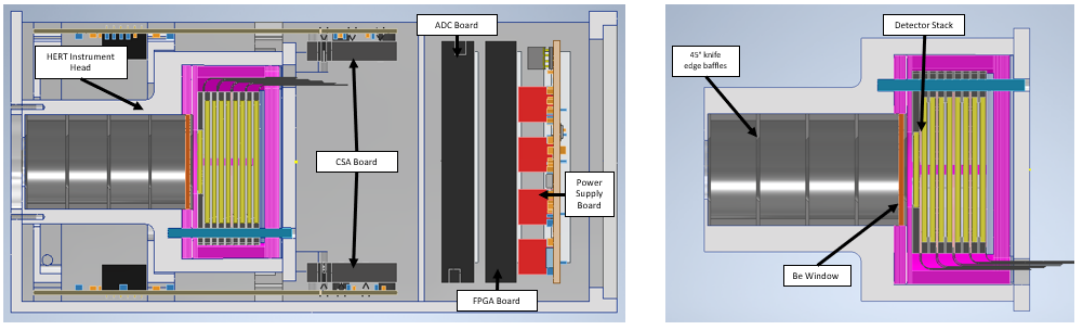

Figure 2.1: RIGHT: Cross-section of HERT Instrument LEFT:Cross-section of HERT Instrument Head

detector to be registered. Based on the amount of total deposited energy in the detector stack, particles are binned to a particular channel if several logic conditions are followed. First, to limit particles that penetrate the shielding from registering as a valid event, an electron must trigger the first detector (deposit energy above the threshold) to be registered. For this reason, the first detector is smaller in diameter compared to the rest of the detectors. This reduces the number of non-FOV particles that do not travel down the boresight being registered as valid events while ensuring all FOV particles that travel through the first detector will be captured by the rest of the detector stack. The first detector is also larger than the collimator opening to ensure it will capture all FOV particles that travel through the collimator. Second, an electron that triggers the last detector (deposits energy above the threshold) will be discarded. The last detector in the stack is utilized as a veto-detector to protect against back-penetrating particles as well as exclude high energy electrons ($\geq$7.5 MeV) that would pass through the entire detector stack.

The number of channels and their deposited energy ranges need to be selected carefully to fulfill instrument requirements. There are several trade-offs in energy channel selections such as narrower energy channels will provide higher energy resolution at the sacrifice of the count rate while wider energy channels sacrifice energy resolution but yield better counting statistics. For this study, forty energy channels were used. Twenty-eight channels with a logarithmic spacing measure deposited energy from 0.5 MeV to 3.0 MeV. These channels are narrower to provide greater energy resolution for HERT's targeted electron population. Ten channels with a logarithm spacing measure deposited energy from 3.0 MeV to 7.0 MeV. These are slightly

wider as fewer high-energy electrons are in the outer radiation belt. These 38 channels form the core energy channels of the HERT instrument. In addition, to make the best use of the low energy threshold of the detectors, two lower energy channels were included to capture electrons that barely get through the beryllium window and deposit small amounts of energy. These two channels with a logarithmic spacing measure deposited energy from 0.1 MeV to 0.5 MeV. They are designed to be quite broad compared to the other 38 channels channels. A full table of energy channels and the corresponding deposited energy ranges can be found in the Appendix.

Chapter 3

Geant4 Simulation Setup

Following work by Yando [29] and Khoo[30], Geant4 (GEometry ANd Tracking 4) version 10.07 was used for instrument characterization. Geant4 is a simulation toolkit that allows HERT to be built virtually and allows users to simulate particles interacting with the instrument and the energy deposited onto each detector. A particle source can be defined with variety of input parameters such as given energy range, source shape, and angle distribution. Following previous literature [29, 30], a spherical particle source centered on the middle of first detector with a radius of 85 mm was initially selected for instrument categorization in a more realistic particle environment (Figure 3.1 left panel). The angular distribution from the source is a cosine distribution so that the particle flux inside the source sphere is isotropic. From this spherical source, particles are given a specific initial energy while initial location on the sphere and particle direction are randomized. For each particle generated, the particle trajectory is simulated, and the energy deposited in each detector is recorded. From this recorded data, the count rate is determined based upon the previously discussed user-defined energy channels, detector threshold, and logic conditions. Electrons are simulated individually, so pileup effects are not accounted for in this study. Simulations were conducted with electrons having energy ranging from 0.5 to 8 MeV.

However, simulating particles from the entire sphere is computationally expensive as billions of particles will need to be simulated to obtain statistically sufficient counts for instrument characterization. A vast majority of the simulated particles from the sphere will not reach the detector stack as they are outside the instrument's FOV and are blocked by the instrument shielding. Thus, instead of simulating an entire sphere, a novel technique of constraining the

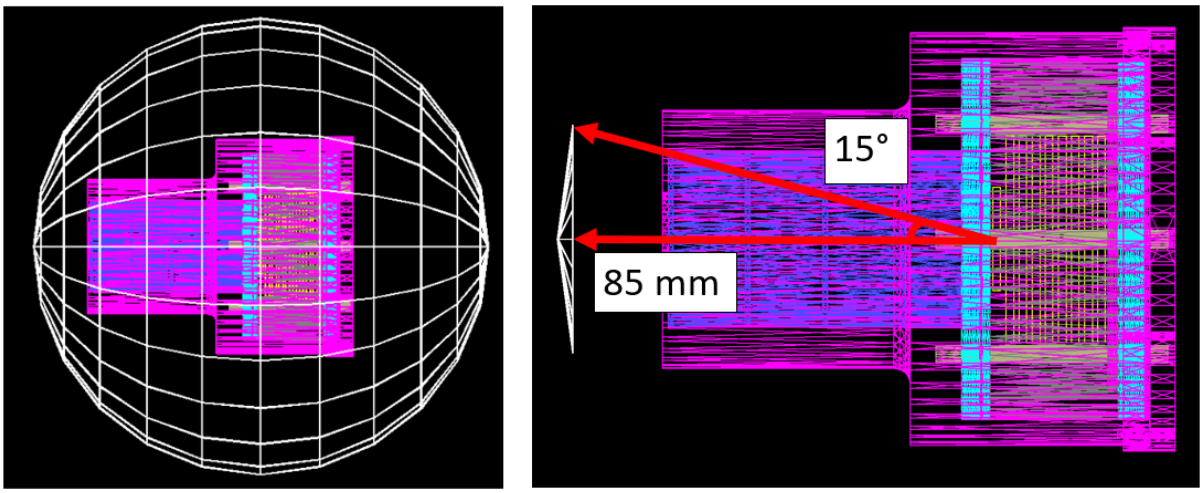

Figure 3.1: LEFT: Geant4 Simulation with Spherical Source RIGHT: Geant4 Simulation with Spherical Cap Source

particle source to a spherical cap was developed (Fig. 3.1 right panel). The spherical cap is a subset of the original sphere that covers the entire FOV and is made with the assumption that all particles contributing to counts are generated from this cap. Likewise, this assumes that the instrument shielding blocks all the particles from the rest of the original sphere. A 15° spherical cap was used in this study as it adequately covers the bore-sight of the instrument. Two million particles for each incident energy from 0.5 MeV to 8.0 MeV with a 0.02 MeV step were simulated from the 15°spherical cap, totaling $\sim$750 million simulated particles. If using a spherical particle source, $\sim$117 times more electrons would be needed to achieve similar statistics. Thus, a main advantage of the spherical cap method is that Geant4 simulation can be conducted more efficiently to provide insight during instrument design and accommodate changes in the design process. For example, Geant4 simulation with a spherical cap particle source was used in HERT design phase in deciding if the detector stack would have anti-coincidence rings. More detail about this can be seen in the Chapter 5. A detailed comparison between the spherical and spherical cap source is provided in Chapter 4 for selected incident energies to validate the spherical cap method.

Chapter 4

Instrument Characterization

4.1 Geometric Factor Calculation

To characterize instrument performance, the geometric factor is often used, which allows the observed count rate of the instrument to be converted to the desired electron flux measurements. In its simplest form, this relationship can be expressed by:

$$C(E) = G(E) * I(E) \tag{4.1}$$

where E is the electron energy, C is the count rate (count sec^{-1}), G is the geometric factor (cm^2 sr), and I is the particle flux (count cm^{-2} s^{-1} sr^{-1})

The Geant4 simulation results can be used to calculate the geometric factor of the instrument. Based on the logic conditions and deposited energy results from Geant4, each simulated particle can be registered as a valid hit in one of the energy channels or be discarded. The geometric factor of energy channel i can be calculated using Geant4 simulation with a spherical particle source as [29]:

$$G_i(E) = \frac{n_i(E) * 4\pi r^2}{N(E)} \tag{4.2}$$

where E is the incident energy of simulated particles, $N(E)$ is the number of particles simulated at incident energy E from the sphere, r is the radius of the sphere, $n_i(E)$ is the number of registered hits in energy channel i of particles with incident energy E.

For the spherical cap source, the above equation is modified to accommodate a scaling factor:

$$G_i(E) = \frac{n_i(E) * 4\pi r^2 * (1 - \cos\theta)}{2 * N'(E)} \tag{4.3}$$

where $N'(E)$ is the number of particles simulated at incident energy E from the spherical cap source and θ is the polar angle of the spherical cap (=15° in this work). This implicitly assumes that particles originating outside of the spherical cap source will be blocked by the instrument shielding.

Using these equations, the geometric factor for each energy channel as a function of energy can be determined, and in turn, the total geometric factor for the instrument, $G(E)$, can be derived by summing the channel results: $G(E) = \sum_i G_i(E)$. Fig. 4.1 shows the total geometric factor of the instrument, $G(E)$, calculated using Geant4 simulation with a spherical cap particle source (black curve). As shown in Figure 4.1, from ∼0.5 MeV to ∼1.5 MeV, the geometric factor from Geant4 with a spherical cap particle source shows a ramp-up feature, indicating the effect of the beryllium window blocking out a portion of lower energy electrons. From ∼1.5 MeV to ∼7.0 MeV, this geometric factor reaches ∼0.2 cm^2sr, with a small positive gradient with energy. This could be from a higher energy particle being more likely to pass through the collimator shielding and deposit sufficient energy on the detector stack. This could also be related to the scattering of the non-FOV electrons as they enter the collimator. From ∼7 MeV to ∼8 MeV, there is a noticeable decline of geometric factor in the spherical cap results approaching the theoretical minimum. This can be caused by the particles of this energy reaching the veto detector and being discarded. Additionally, the selection of energy channels is only recording events with ≤7 MeV of deposited energy, so certain electrons of ≥7 MeV are discarded as they deposit energy over this threshold. These two occurrences together form the decline seen ∼7 MeV to ∼8 MeV.

As a benchmark to the Geant4 calculated results, the theoretical geometric factor as presented by Sullivan [31] was used for comparison. Sullivan shows how the geometric factor of an instrument can be expressed to be only dependent on the physical geometry of the instrument.

This requires several assumptions such as ideal detector response and straight-line particle trajectories (i.e. no particle scattering). For a circular symmetrical telescope such as HERT, the instrument can be simplified into a series of discs to analytically evaluate the geometric factor. Each detector and collimator tooth can be expressed as a disc for a total of fourteen discs. Following Sullivan (1971)'s example, this series of discs can be reduced to only consider the discs that are constraining the geometric factor. For example, because the first detector is smaller in diameter, it is the only detector that impacts the geometric factor as every FOV particle that passes through the first detector will subsequently travel through the rest of the detector stack. Additionally, the collimator teeth have the same opening diameter. Therefore, only the first and last tooth need to be considered. As a result, even though the telescope can be represented by fourteen discs, only three discs constrain the geometric factor: the first collimator tooth, the last collimator tooth, and the first detector. Detailed geometry of the three discs determines which two are the limiting factors in the geometric factor calculation. From Sullivan[31], the theoretical geometric factor for a two-disc telescope is easily calculated using the radius of the two discs and the length between them by:

$$G = \frac{\pi^2}{2} * [R_1^2 + R_2^2 + l^2 - ((R_1^2 + R_2^2 + l^2)^2 - 4 * R_1^2 * R_2^2)^{\frac{1}{2}}] \tag{4.4}$$

where R_1 is the radius of the first disc, R_2 is the radius of the second disc, and l is the length between the two of discs.

Fig. 4.1 also shows the theoretical geometric factors of the instrument using Eq. 4.4 to compare with that from Geant4 simulation. The minimum theoretical geometric factor (green dashed line) was found by assuming the knife edge collimator teeth blocks every particle. In this case, since the first detector is sufficiently close to the last collimator tooth and the detector area is larger, it no longer constrains the geometric factor as every FOV particle that passes through the last tooth will reach the first detector. Thus, only the collimator determines the theoretical geometric factor which is then represented by a two-disc circularly symmetric telescope. From Eq. 4.4, this results in R1 of 0.9 cm, R2 of 0.9 cm, and l of 6.0 cm for a theoretical geometric factor of 0.17221 cm^2sr. The maximum theoretical geometric factor (blue dashed line) was

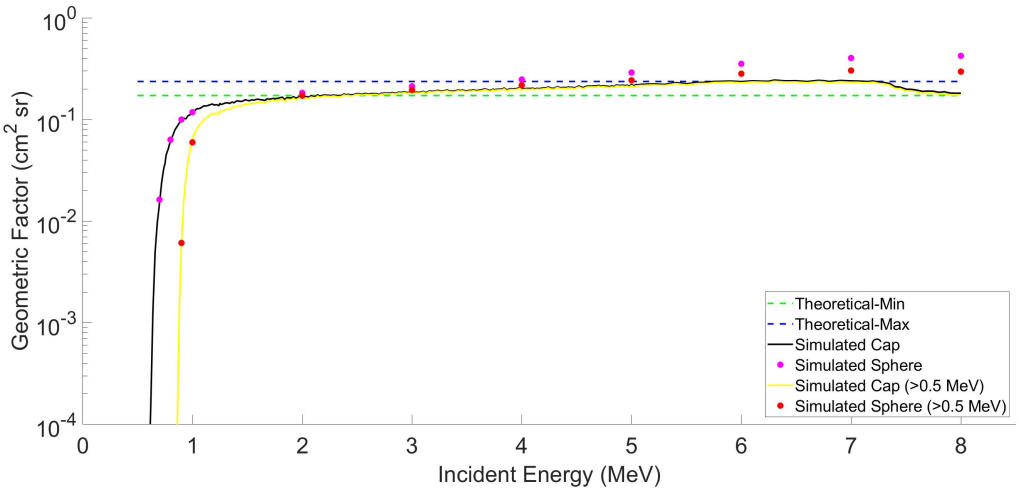

Figure 4.1: Total Geometric Factor for Theoretical, Spherical Cap Simulation and Full Spherical Simulation.

found by assuming the knife edge does not block any particles, thus increasing the collimator opening used in Eq. 4.4. This aligns more with what is expected at higher energies. Increasing the opening changes the constraining geometry for the theoretical calculation. With this, the first detector and first collimator tooth now determine the theoretical geometric factor, and the larger opening leads to a larger geometric factor. From Eq. 4.4, this results in R1 of 1.0 cm, R2 of 1.0 cm, and l of 6.3 cm for a theoretical geometric factor of 0.237 cm2sr.

In general, the geometric factor calculated using Geant4 simulation with a spherical cap particle source (black curve) fits well with the theoretical results at the targeted energy range. The Geant4 geometric factor surpasses the minimum theoretical value at $\sim$2 MeV. This indicates that the Beryllium window and tantalum collimator are effective at blocking particles up to that energy. From $\sim$2 MeV to $\sim$6 MeV, the Geant4 geometric factor is between the two theoretical values, indicating that higher energy non-FOV electrons have a greater chance to pass through the knife-edge of collimator baffles and register as hits. From $\sim$6 MeV to $\sim$7 MeV, the spherical cap geometric factor matches or slightly surpasses the maximum theoretical factor where the tantalum collimator is not blocking as many non-FOV particles and the assumptions made when calculating the theoretical values are not strictly valid. From $\sim$7 MeV to 8 MeV, the difference between the two increases with the decline in cap results that was previously discussed.

Comparing the results from the two Geant4 simulation setups with the spherical cap source (black curve) and the full spherical source (magenta dots) in Fig. 4.1, there is good agreement at low energy with almost identical ramp up behavior until approximately 2 MeV. From 2 MeV upwards to $\sim$7 MeV, there is an increasing deviation as higher energy electrons from the sperical source become more likely to pass through the instrument shielding and deposit sufficient energy to be registered as a hit. From $\sim$7 MeV to 8 MeV, the difference between the two simulations increases as the decline in cap results is not seen in the full spherical results. This is further indication of non-FOV particles from the spherical source passing through the shielding and registering as hits.

The Geant4 results shown in a black curve or magenta dots in Fig. 3 include all energy channels with deposited total energy ranges from 0.1 to 7 MeV. If we exclude the first two energy channels which are designed to capture low-energy electrons that barely go through the beryllium window and deposit 0.1 – 0.5 MeV energy, the agreement at higher incident energies from the spherical cap and spherical solutions improves, which can also be seen in Fig. 4.1 (yellow curve and red dots). This shows that a majority of the multi-MeV particles from the spherical simulation barely penetrate through the instrument shielding and deposit no more than 0.5 MeV in the detector stack. The great agreement between the spherical cap and spherical source simulation as well as the between the Geant4 simulation and theoretical values validates the Geant4 simulation with a spherical cap simulation as a cost-efficient method to provide accurate characterization of instrument performance, especially for HERT core energy channels.

Fig. 4.2 shows the geometric factor as a function of incident energy from the spherical cap Geant4 simulation for each of the forty energy channels with select channels highlighted. Each curve represents the geometric factor of one energy channel. As previously discussed, the first two energy channels are quite broad compared to the other thirty-eight channels. Each energy channel has a defined peak of incident energy but also has a distinct tail. The peak indicates the energy of a particle that is most likely to be binned in a specific channel. Channel 2 has a larger peak compared to other channels as it is relatively wider. Channel 1 does not have this large peak as it is measuring at very low energy (0.1-0.22 MeV) that is usually lost in the Be window. The tail leads to sizeable overlap between the energy channels, and these tails are caused by

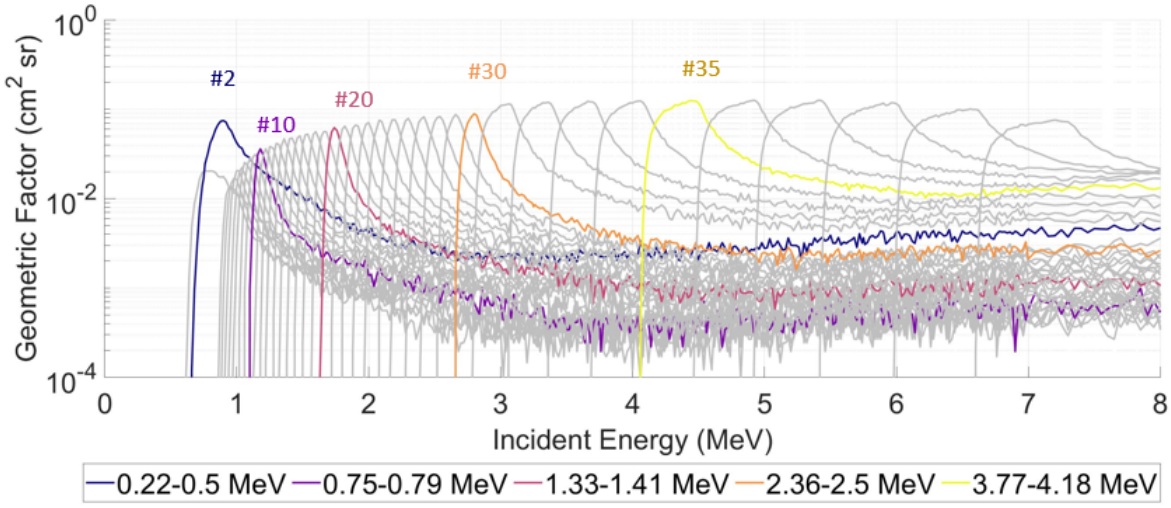

Figure 4.2: Geometric Factor per Energy Channel as a function of incident energy. Select channels are highlighted with their corresponding deposited energy ranges listed at the bottom

electron scattering or higher energy non-FOV electrons piercing the shielding depositing lower amounts of energy compared to FOV electrons. For example, for channel 20 with a deposited energy range of 1.33 to 1.41 MeV, the peak of incident energy for this channel is at $\sim$1.75 MeV, and the difference between the incident energy and the deposited energy is due to the energy lost as electrons pass through the Be window. However, even an electron with an incident energy of 6 MeV has a small chance of depositing between 1.33 MeV and 1.41 MeV on the detector stack. This is most likely due to the electron scattering off the detector stack. Ideally, there would be a clean transition between the energy channels, and the geometric response function for each channel would resemble a ”sawtooth” or ”box” shape. However, this does not occur due to electrons scattering. Thus, to define the nominal energy and the channel width of each energy channel, bow-tie analysis is conducted.

4.2 Energy Resolution Characterization

With the response functions obtained from Geant4, the Blake-Selesnick bow tie method [32] was utilized to convert the continuous response functions into discrete bins. This method begins by assuming that the count rate of each energy channel r, which is described as the integral of the response function multiplied by the flux over all energies, can be approximated as the product of a set of bin parameters: effective geometric factor (height of the bin) G_{eff}, channel

width ΔE, and the flux at the channel's nominal energy $I(E_{nom})$. This relationship is expressed as:

$$r = \int G(E) * I(E)\, dE \; = G_{eff} * \Delta E * I(E_{nom}) \tag{4.5}$$

The flux profile is assumed to be exponential with $I = I_0 e^{-E/E_o}$, where I_o and E_o are constants. Then, the equation can be simplified to:

$$G_{eff} * \Delta E = e^{E_{nom}/E_o} \int G(E) * e^{-E/E_o}\, dE \tag{4.6}$$

From here, $G_{eff} * \Delta E$ can be plotted as a function of both E_{nom} and E_o. With varying E_o, the resulting curves will form a bow tie shape of which the average intersection point is the best approximation of the nominal energy and the product of $G_{eff} * \Delta E$. The obtained results are reliant on the E_o values selected, and the E_o used in this study ranged from 0.2 to 2.0. These values were selected based on REPT measurements from 2014 to 2015. An example of this plot can be seen the left panel in Fig. 4.3. Then, the Full-Width Half Max (FWHM) method was used to disentangle the effective geometric factor from the channel width. The right panel in Fig. 4.3 shows how the FWHM value is found by using the half-maximum points surrounding the geometric factor peak. The FHWM value is the distance along the x-axis from the two half-maximum points surrounding the geometric factor peak.

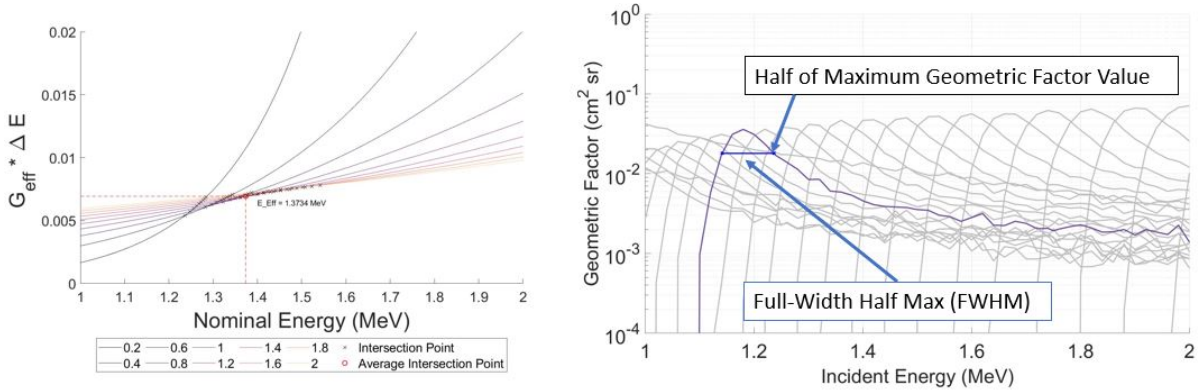

Figure 4.3: LEFT:Bowtie Plot for energy channel 10 with deposited energy range 0.75 MeV-0.79 MeV. Each line uses a different Eo value noted in the legend. RIGHT: Geometric Factor of channel 10 highlighted from 1-2 MeV.

With the response function of each energy channel from Geant4 and bow tie analysis, the channel width and effective geometric factor can be found for each channel. Fig. 4.4 shows the energy resolution (dE/E) of each channel from this analysis. The results show HERT's 38 core energy channels achieve the ten percent energy resolution requirement. For energy channels with a nominal energy between 1.5 MeV and 3 MeV, the energy resolution even reaches ∼5%. These suggest that HERT meets the energy resolution requirements and can provide high-energy-resolution measurements of outer radiation belt electron core population. On the other hand, though with relatively poor resolution, the first two energy channels make the most of the instrument and provide the capability to measure lower-energy electrons at the same time.

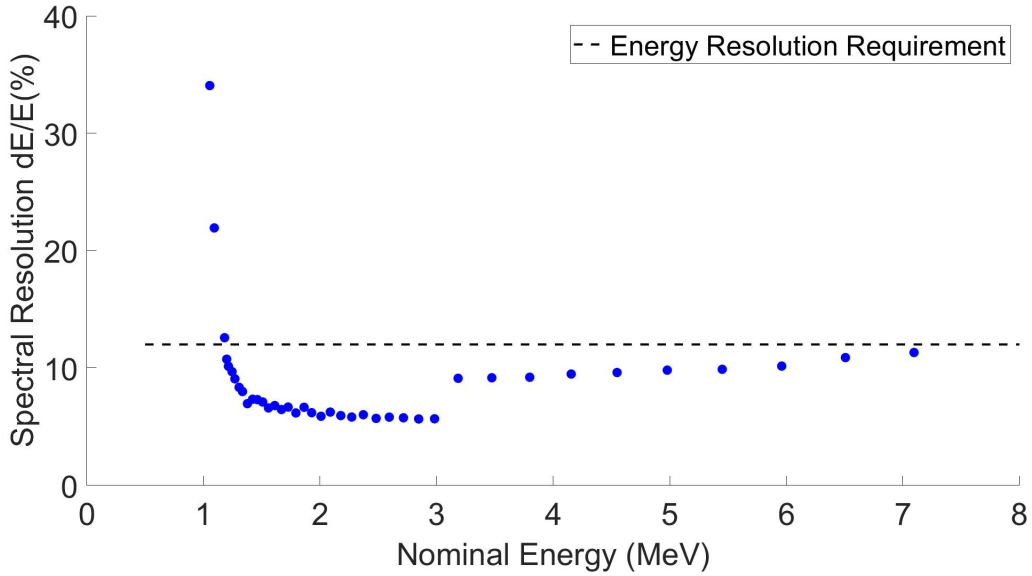

Figure 4.4: Energy Resolution (dE/E) for HERT. Each dot represents a single energy channel

4.3 Count Rate Estimation

While the energy resolution of each channel is important, each energy channel requires statistically sufficient count rates when operating in the outer radiation belt to provide valid science observations. This requires a trade off between narrower channels for better energy resolution and wider channels for greater count rates. On the other hand, the instrument electronics can process five hundred thousand events per second, so counts rates of each detector should remain

below this limit to avoid saturation. In this study, the AE9 radiation belt electron flux model [33] was used to guide the count rate estimation. AE9 provided statistics of fluxes of electrons for energies from 0.5 MeV to 8.0 MeV that a satellite would encounter in GTO at the equatorial plane. Table 4.1 shows the estimated count rate on the 1st detector using AE9 90° pitch angle electron fluxes at various percentiles at the center of the outer radiation belt (L=4) and at GTO apogee (L=6.6). Even at the 95th percentile, these results are below five hundred thousand per second, showing the instrument will not be saturated in most conditions.

Table 4.1: Count Rate on 1st Detector at Apogee and Center of Outer Belt

Count Rate on 1st Detector (count secˆ-1) from AE9 Fluxes				
Location	**25th Percentile**	**50th Percentile**	**75th Percentile**	**95th Percentile**
Apogee (L=6.6)	685.75	2.4952e+03	7.0162e+03	2.2474e4
Center of Outer Belt (L=4)	4.4021e3	1.9091e4	6.1313e4	2.2688e5

Fig. 4.5 shows the expected counted rates for each energy channel with AE9 fluxes from the center of the outer radiation belt (green dots) and at GTO apogee (blue dots). Each dot represents an energy channel, and the x-axis represents the nominal energy determined from bow tie analysis. As expected, the count rates follow a negative exponential with estimated count rates of hundreds or thousands per second at lower energy and only a few counts per second at higher energies. The expected count rates are sufficient with the exception of the last few channels. These channels have very few counts due to the scarcity of these particles in the outer radiation belt, but the statistics can be improved by integrating over a longer time interval for these high-energy channels.

4.4 Side Penetration Tests

Additional Geant4 simulations were conducted to characterize the instrument's shielding capability. In each of these Geant4 runs, a beam particle source was created to launch particles at the side tungsten-epoxy shielding. In the first set of runs, the source was aimed perpendicularly to the side shielding and directed to the first detector. This represents the worse-case scenario for side penetration as a non-FOV particle that passes through the shielding and triggers the first detector would erroneously be recorded as a hit. A second set of Geant4 runs aimed the beam source toward the middle of the entire detector stack perpendicular to the side shielding.

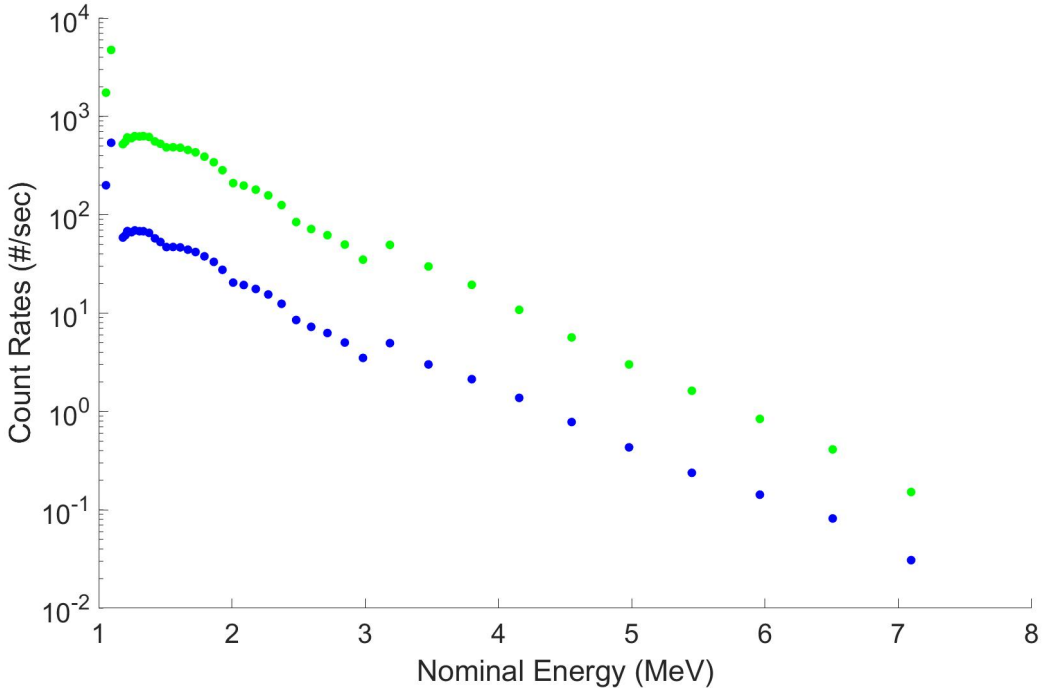

Figure 4.5: Estimated Count Rates for each channel with 50th percentile AE9 fluxes at GTO Apogee (L=6.6) in Blue and center of outer radiation belt (L=4)in Green

Incident energy of electrons from 0.5 to 10 MeV were simulated with the same energy channels and binning logic as previous Geant4 simulations. One hundred thousand electrons were simulated at each incident energy. Fig. 4.6 shows the percentage of particles that were binned as valid hits from each of these simulation setups. It is easy to see as energy increases the percentage of electrons penetrating through the side shielding and being registered as a valid event increases. However, it is still only a fraction of a percent even for 10 MeV electrons for both setups showing the instrument shielding and binning logic are blocking the most majority of side-penetrating particles. Since the back-penetrating particle will be vetoed by the back detector, these side-penetration simulations demonstrate that HERT has sufficient shielding to block non-FOV electrons. This also leads to more confidence in the spherical cap method.

On the other hand, high-energy protons are more likely to penetrate through the side tungsten-epoxy instrument shielding. Geant4 simulation results suggest that almost all protons with incident greater than 65 MeV can penetrate through the side of the instrument and trigger the first detector. However, highly energetic protons are not typically found in the outer

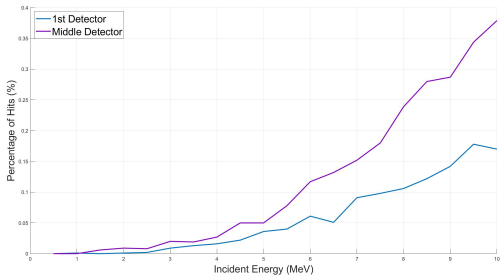

Figure 4.6: Percentage of Hits from Side Penetration electrons as a function of incident energy using Geant4 Simulation

radiation belts, so HERT measurements of outer belt electrons would not likely be influenced by proton contamination. One exception is that during solar proton events, 10s – 100s MeV proton fluxes could enhance temporarily in the outer radiation belt, contaminating electron measurements. However, these events happen relatively infrequently in the inner magnetosphere [34], so they do not pose a significant risk of affecting the electron measurements.

Chapter 5

Discussion on Geant4 simulation for Instrument Design

Geant4 was utilized for designing the instrument in addition to instrument characterization. During the design process, two different detector stack configurations were simulated to decide what would be optimal. The difference between the configurations were the use of anti-coincidence rings. The ”whole” configuration has a first detector with a 20 mm diameter followed by 8 detectors of 40 mm in diameter matching the design show in the previous chapters. The inner configuration had eight 20 mm detectors surrounded by a series of anti-coincidence rings followed by 40mm detector for a total of 19 active areas. Each configuration used the last detector in the stack as a veto detector for over-penetrating particles and required the first detector to be triggered. The inner configuration extended this veto logic to the eight anti-coincidence rings. If any of these rings were triggered, the event would be discarded. This protects against scattering electrons that don't deposit all of their energy in the detector stack as well as side-penetrating electrons. A schematic for the two detector configurations can be seen in Fig. 5.1.

These two configurations were simulated in Geant4 using the same spherical cap process and energy channels presented previously. The geometric factor calculations for each configuration were also calculated using the same methods. Additionally, the theoretical geometric factors were calculated for the inner version using the same procedure from Sullivan[31]as a benchmark. Because each detector in the inner configuration is the same size, the theoretical geometric factor is now dependent on incident energy as higher energy electrons would need to pass through more detectors without scattering to the anti-coincidence rings to be recorded as an event. It was assumed that a 1 MeV electron would reliably reach the first detector and that

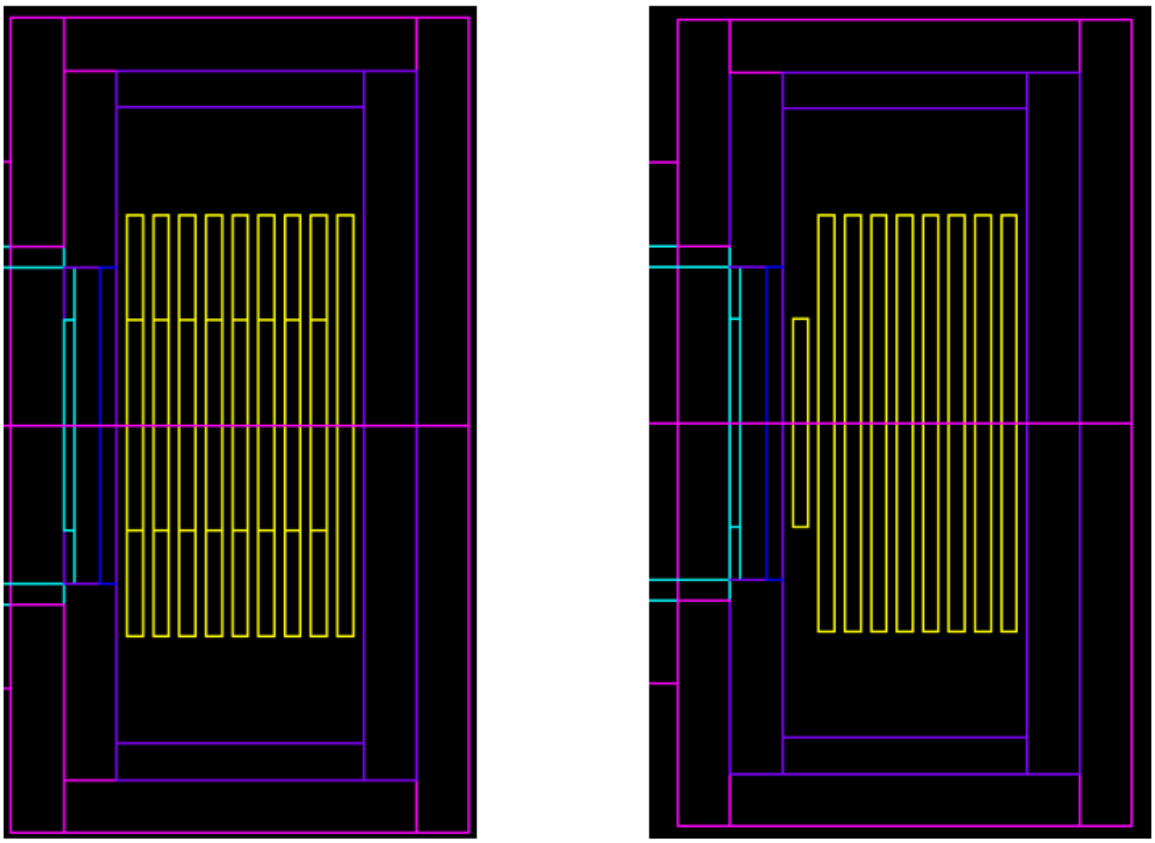

Figure 5.1: Inner (Right Panel) vs. Whole (Left Panel) Configuration Comparison

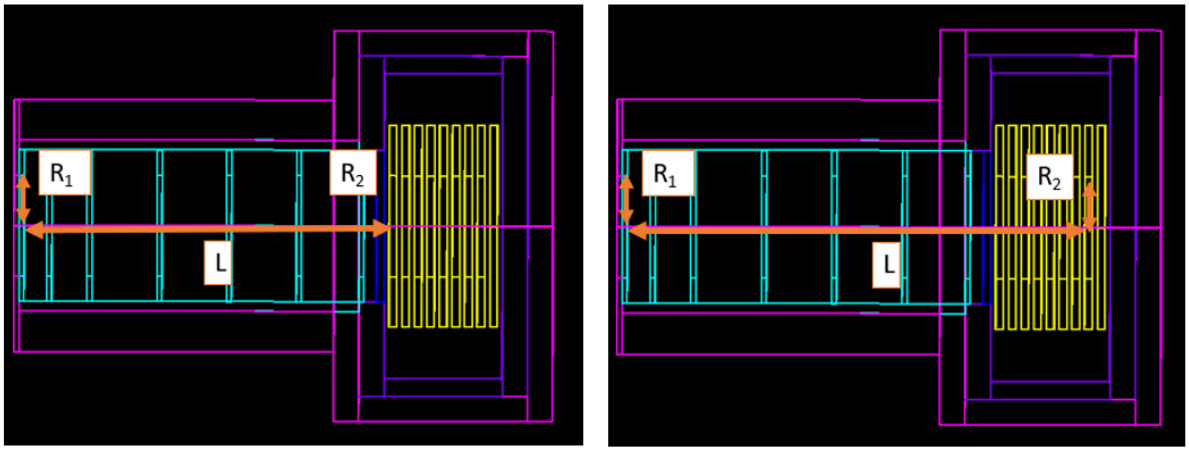

Figure 5.2: Inner Theoretical Calculation. LEFT: Theoretical calculation at lower energies. RIGHT: Theoretical calculation at higher energies.

a 7 MeV particle would reach the 8th detector. These provide the two points for calculating the energy dependent geometric factor, and the rest were found by interpolating using a linear fit. Fig. 5.2 shows the geometry used for the values required for the theoretical geometric factor [31]. Please note, the collimator design in these particular Geant4 simulations is different from the previous chapter(s) as collimator design was not finalized at the time of the simulations discussed in this chapter. The length of the collimator is 6.85 cm in length with an opening of 1.0 cm. The collimator is longer but has a larger opening with a net result of a larger minimum theoretical geometric factor of 0.20182 cm^2sr. The result of a larger geometric factor will be more count rates compared to previous chapters. Fig. 5.3 shows the results from the two Geant4 simulation setups and theoretical calculations. The inner configuration shows good agreement with the theoretical calculation. As expected, below 1 MeV, it matches with the whole configuration as the beryllium window is blocking the majority of these particles. From 1 to $\sim$2.5 MeV, Geant4 results for the inner configuration are slightly above the inner theoretical value. This matches the results from the whole configuration compared to its theoretical calculations. However, from $\sim$2.5 MeV to $\sim$8 MeV, Geant4 results are below the theoretical min. This can explained by high-energy electrons scattering triggering the anti-coincidence rings which is not accounted for in the theoretical calculation. Fig. 5.4 shows the geometric factor of each energy channel from the inner configuration. Table A.4 shows the results from Bow-Tie analysis for the inner configuration. These results allow for estimated count rate calculation as shown

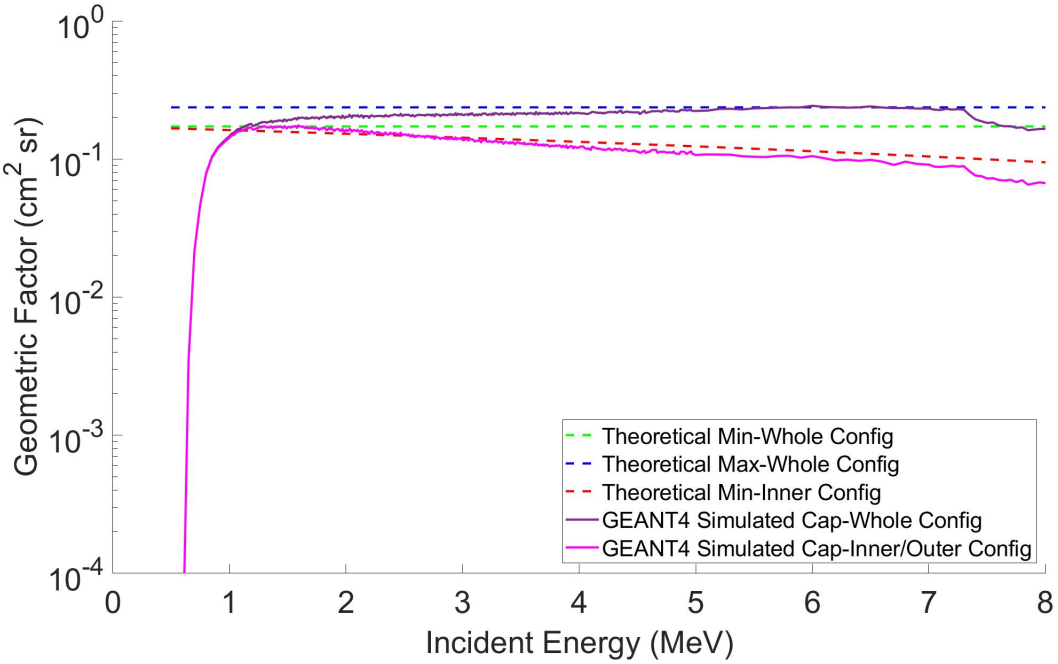

Figure 5.3: Whole vs. Inner Comparison. Geant4 results in solid lines while theoretical calculations in dashed lines.

previously, and the expected count rates are lower than the whole configuration especially at higher energies with less expected particles in GTO. These count rates can be seen in Table A.5 and Table A.6 which shows the expected count rates at L = 4 and L = 6.6 for a variety of fluxes provided by AE9 for each configuration. Due to this, the inner configuration was discarded as it would not have the the count rates sufficient at higher energies. In addition, side-penetration tests seen previously had shown sufficient results to forgo anti-coincidence rings. The whole configuration provides a less complex and cheaper detector stack while not sacrificing performance. In conclusion, Geant4 simulation using the spherical cap greatly informed the detector stack of HERT by allowing more efficient instrument characterization during the design process.

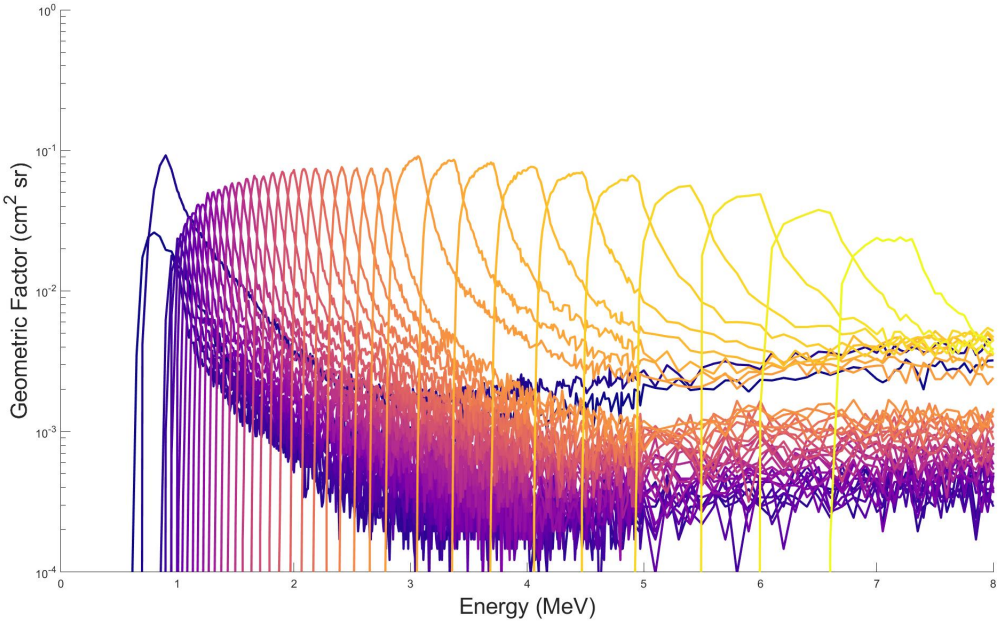

Figure 5.4: Inner Configuration: Geometric Factor for each energy channel. Each curve is a single energy channel.

Chapter 6

Conclusion

HERT is a miniaturized particle telescope designed to measure 1-7 MeV electrons in Earth's outer radiation belt with high energy resolution. Using a novel efficient setup of Geant4 simulation with a spherical cap particle source, HERT's instrument performance is characterized, and the geometric factor is calculated. The geometric factor for HERT was also validated against those calculated using a spherical source in Geant4 and theoretical methods. From the geometric factor results, energy resolution for the forty energy channels was found using bow-tie analysis in conjunction with the FWHM method. These results show that HERT will meet the ten percent requirement for its core channels and have statistically sufficient count rates without over-saturating instrument electronics. In addition, side penetration simulations were conducted and show HERT's shielding is sufficient to block the most non-FOV electrons. In conclusion, as a miniaturized instrument, HERT will be able to achieve the energy resolution required for its science objectives at GTO and significantly contribute to the quantitative understanding of the radiation belt electron dynamics.

References

[1] Tzu-Wei Fang, Adam Kubaryk, David Goldstein, Zhuxiao Li, Tim Fuller-Rowell, George Millward, Howard J. Singer, Robert Steenburgh, Solomon Westerman, and Erik Babcock. Space Weather Environment During the SpaceX Starlink Satellite Loss in February 2022. *Space Weather*, 20(11), November 2022.

[2] Christine Gabrielse, Justin H. Lee, Seth Claudepierre, Don Walker, Paul O'Brien, James Roeder, Yao Lao, Jann Grovogui, Drew L. Turner, Andrei Runov, Alexander Boyd, Joseph Fennell, J. Bernard Blake, Kevin Lopez, Yoshizumi Miyoshi, Kunihiro Keika, Nana Higashio, Iku Shinohara, Shun Imajo, Satoshi Kurita, and Takefumi Mitani. Radiation Belt Daily Average Electron Flux Model (RB-Daily-E) From the Seven-Year Van Allen Probes Mission and Its Application to Interpret GPS On-Orbit Solar Array Degradation. *Space Weather*, 20(11), November 2022.

[3] D. N. Baker, P. J. Erickson, J. F. Fennell, J. C. Foster, A. N. Jaynes, and P. T. Verronen. Space Weather Effects in the Earth's Radiation Belts. *Space Science Reviews*, 214(1):17, February 2018.

[4] Solène Lejosne and Peter Kollmann. Radiation Belt Radial Diffusion at Earth and Beyond. *Space Science Reviews*, 216(1):19, February 2020.

[5] G. D. Reeves, H. E. Spence, M. G. Henderson, S. K. Morley, R. H. W. Friedel, H. O. Funsten, D. N. Baker, S. G. Kanekal, J. B. Blake, J. F. Fennell, S. G. Claudepierre, R. M. Thorne, D. L. Turner, C. A. Kletzing, W. S. Kurth, B. A. Larsen, and J. T. Niehof. Electron Acceleration in the Heart of the Van Allen Radiation Belts. *Science*, 341(6149):991–994, August 2013.

[6] R. M. Thorne, W. Li, B. Ni, Q. Ma, J. Bortnik, L. Chen, D. N. Baker, H. E. Spence, G. D. Reeves, M. G. Henderson, C. A. Kletzing, W. S. Kurth, G. B. Hospodarsky, J. B. Blake, J. F. Fennell, S. G. Claudepierre, and S. G. Kanekal. Rapid local acceleration of relativistic radiation-belt electrons by magnetospheric chorus. *Nature*, 504(7480):411–414, December 2013.

[7] B. H. Mauk, N. J. Fox, S. G. Kanekal, R. L. Kessel, D. G. Sibeck, and A. Ukhorskiy. Science Objectives and Rationale for the Radiation Belt Storm Probes Mission. In Nicola Fox and James L. Burch, editors, *The Van Allen Probes Mission*, pages 3–27. Springer US, Boston, MA, 2012.

[8] D. N. Baker, S. G. Kanekal, V. C. Hoxie, S. Batiste, M. Bolton, X. Li, S. R. Elkington, S. Monk, R. Reukauf, S. Steg, J. Westfall, C. Belting, B. Bolton, D. Braun, B. Cervelli, K. Hubbell, M. Kien, S. Knappmiller, S. Wade, B. Lamprecht, K. Stevens, J. Wallace, A. Yehle, H. E. Spence, and R. Friedel. The Relativistic Electron-Proton Telescope (REPT) Instrument on Board the Radiation Belt Storm Probes (RBSP) Spacecraft: Characterization of Earth's Radiation Belt High-Energy Particle Populations. In Nicola Fox and James L. Burch, editors, *The Van Allen Probes Mission*, pages 337–381. Springer US, Boston, MA, 2014.

[9] Daniel N. Baker, Vaughn Hoxie, Hong Zhao, Allison N. Jaynes, Shri Kanekal, Xinlin Li, and Scot Elkington. Multiyear Measurements of Radiation Belt Electrons: Acceleration, Transport, and Loss. *Journal of Geophysical Research: Space Physics*, 124(4):2588–2602, April 2019.

[10] H. Zhao, D. N. Baker, S. Califf, X. Li, A. N. Jaynes, T. Leonard, S. G. Kanekal, J. B. Blake, J. F. Fennell, S. G. Claudepierre, D. L. Turner, G. D. Reeves, and H. E. Spence. Van Allen Probes Measurements of Energetic Particle Deep Penetration Into the Low L Region ($L < 4$) During the Storm on 8 April 2016. *Journal of Geophysical Research: Space Physics*, 122(12), December 2017.

[11] H. Zhao, D. N. Baker, X. Li, A. N. Jaynes, and S. G. Kanekal. The Effects of Geomagnetic Storms and Solar Wind Conditions on the Ultrarelativistic Electron Flux Enhancements. *Journal of Geophysical Research: Space Physics*, 124(3):1948–1965, March 2019.

[12] H. Zhao, D. N. Baker, X. Li, A. N. Jaynes, and S. G. Kanekal. The Acceleration of Ultrarelativistic Electrons During a Small to Moderate Storm of 21 April 2017. *Geophysical Research Letters*, 45(12):5818–5825, June 2018.

[13] H. Zhao, D.N. Baker, X. Li, D.M. Malaspina, A.N. Jaynes, and S.G. Kanekal. On the Acceleration Mechanism of Ultrarelativistic Electrons in the Center of the Outer Radiation Belt: A Statistical Study. *Journal of Geophysical Research: Space Physics*, 124(11):8590–8599, November 2019.

[14] D. N. Baker, H. Zhao, X. Li, S. G. Kanekal, A. N. Jaynes, B. T. Kress, J. V. Rodriguez, H. J. Singer, S. G. Claudepierre, J. F. Fennell, and V. Hoxie. Comparison of Van Allen Probes Energetic Electron Data With Corresponding GOES-15 Measurements: 2012–2018. *Journal of Geophysical Research: Space Physics*, 124(12):9924–9942, December 2019.

[15] Michael Schulz and Louis J. Lanzerotti. Pitch-Angle Diffusion. In J. G. Roederer, editor, *Particle Diffusion in the Radiation Belts*, volume 7, pages 46–80. Springer Berlin Heidelberg, Berlin, Heidelberg, 1974. Series Title: Physics and Chemistry in Space.

[16] Theodore E. Sarris, Xinlin Li, Michael Temerin, Hong Zhao, Sam Califf, Wenlong Liu, and Robert Ergun. On the relationship between electron flux oscillations and ULF wave-driven radial transport. *Journal of Geophysical Research: Space Physics*, 122(9):9306–9319, September 2017.

[17] Theodore E. Sarris, Xinlin Li, Michael Temerin, Hong Zhao, Leng Ying Khoo, Drew L. Turner, Wenlong Liu, and Seth G. Claudepierre. Simulations of Electron Flux Oscillations as Observed by MagEIS in Response to Broadband ULF Waves. *Journal of Geophysical Research: Space Physics*, 125(7):e2020JA027798, 2020.

[18] Theodore E. Sarris, Xinlin Li, Hong Zhao, Leng Ying Khoo, Wenlong Liu, and Michael A. Temerin. On the Association Between Electron Flux Oscillations and Local Phase Space Density Gradients. *Journal of Geophysical Research: Space Physics*, 126(2), February 2021.

[19] Hong Zhao, Theodore E. Sarris, Xinlin Li, Max Weiner, Isabela G. Huckabee, Daniel N. Baker, Allison J. Jaynes, Shrikanth G. Kanekal, Scot R. Elkington, Mohammad Barani, Weichao Tu, Wenlong Liu, Dianjun Zhang, and Michael D. Hartinger. Van Allen Probes Observations of Multi-MeV Electron Drift-Periodic Flux Oscillations in Earth's Outer Radiation Belt During the March 2017 Event. *Journal of Geophysical Research: Space Physics*, 126(8):e2021JA029284, 2021.

[20] Hong Zhao, Theodore E. Sarris, Xinlin Li, Isabella G. Huckabee, Daniel N. Baker, Allison J. Jaynes, and Shrikanth G. Kanekal. Statistics of Multi-MeV Electron Drift-Periodic Flux Oscillations Using Van Allen Probes Observations. *Geophysical Research Letters*, 49(7), April 2022.

[21] M. D. Hartinger, G. D. Reeves, A. Boyd, M. G. Henderson, D. L. Turner, C. M. Komar, S. G. Claudepierre, I. R. Mann, A. Breneman, S. Di Matteo, and X.-J. Zhang. Why Are There so Few Reports of High-Energy Electron Drift Resonances? Role of Radial Phase Space Density Gradients. *Journal of Geophysical Research: Space Physics*, 125(8), August 2020.

[22] T. P. O'Brien, J. C. Green, A. J. Halford, B. P. Kwan, S. G. Claudepierre, and Louis G. Ozeke. Drift Phase Structure Implications for Radiation Belt Transport. *Journal of Geophysical Research: Space Physics*, 127(8), August 2022.

[23] D. N. Baker, S. G. Kanekal, V. C. Hoxie, S. Batiste, M. Bolton, X. Li, S. R. Elkington, S. Monk, R. Reukauf, S. Steg, J. Westfall, C. Belting, B. Bolton, D. Braun, B. Cervelli, K. Hubbell, M. Kien, S. Knappmiller, S. Wade, B. Lamprecht, K. Stevens, J. Wallace, A. Yehle, H. E. Spence, and R. Friedel. The Relativistic Electron-Proton Telescope

(REPT) Instrument on Board the Radiation Belt Storm Probes (RBSP) Spacecraft: Characterization of Earth's Radiation Belt High-Energy Particle Populations. *Space Science Reviews*, 179(1-4):337–381, November 2013.

[24] Daniel N. Baker, Shrikanth G. Kanekal, Vaughn Hoxie, Xinlin Li, Allison N. Jaynes, Hong Zhao, Scot R. Elkington, John C. Foster, Richard Selesnick, Binbin Ni, Harlan Spence, and Rachel Filwett. The Relativistic Electron-Proton Telescope (REPT) Investigation: Design, Operational Properties, and Science Highlights. *Space Science Reviews*, 217(5):68, August 2021.

[25] Quintin G Schiller, Abhishek Mahendrakumar, and Xinlin Li. REPTile: A Miniaturized Detector for a CubeSat Mission to Measure Relativistic Particles in Near-Earth Space. *In Proceedings of the 24th annual AIAA/USU conference on small satellites*, 2010.

[26] Quintin Schiller, David Gerhardt, Lauren Blum, Xinlin Li, and Scott Palo. Design and scientific return of a miniaturized particle telescope onboard the Colorado Student Space Weather Experiment (CSSWE) CubeSat. In *2014 IEEE Aerospace Conference*, pages 1–14, March 2014. ISSN: 1095-323X.

[27] X. Li, Q. Schiller, L. Blum, S. Califf, H. Zhao, W. Tu, D. L. Turner, D. Gerhardt, S. Palo, S. Kanekal, D. N. Baker, J. Fennell, J. B. Blake, M. Looper, G. D. Reeves, and H. Spence. First results from CSSWE CubeSat: Characteristics of relativistic electrons in the near-Earth environment during the October 2012 magnetic storms. *Journal of Geophysical Research: Space Physics*, 118(10):6489–6499, October 2013.

[28] Lucimara Scaduto. Baffle Design and Analysis of Stray-light in Multispectral Camera of a Brazilian Satellite. January 2023.

[29] Karl Yando, Robyn M. Millan, Janet C. Green, and David S. Evans. A Monte Carlo simulation of the NOAA POES Medium Energy Proton and Electron Detector instrument. *Journal of Geophysical Research: Space Physics*, 116(A10), 2011.

[30] L.-Y. Khoo, X. Li, R. S. Selesnick, Q. Schiller, K. Zhang, H. Zhao, B. Hogan, J. T. Cantilina, A. Sims, E. Bauch, T. Valade, S. Boyajian, and R. Kohnert. On the Challenges of Measuring Energetic Particles in the Inner Belt: A Geant4 Simulation of an Energetic Particle Detector Instrument, REPTile-2. *Journal of Geophysical Research: Space Physics*, 127(4):e2021JA030249, 2022.

[31] J. D. Sullivan. Geometric factor and directional response of single and multi-element particle telescopes. *Nuclear Instruments and Methods*, 95(1):5–11, August 1971.

[32] R. S. Selesnick and J. B. Blake. On the source location of radiation belt relativistic electrons. *Journal of Geophysical Research: Space Physics*, 105(A2):2607–2624, 2000.

[33] G. P. Ginet, T. P. O'Brien, S. L. Huston, W. R. Johnston, T. B. Guild, R. Friedel, C. D. Lindstrom, C. J. Roth, P. Whelan, R. A. Quinn, D. Madden, S. Morley, and Yi-Jiun Su. AE9, AP9 and SPM: New Models for Specifying the Trapped Energetic Particle and Space Plasma Environment. *Space Science Reviews*, 179(1-4):579–615, November 2013.

[34] Rachael Filwett, Allison Jaynes, and Brian Kress. Statistical Study of Solar Energetic Proton Access during the Van Allen Probes Era. In *AGU Fall Meeting Abstracts*, volume 2021, pages SM15B–1974, December 2021.

Appendices

Appendix A

Energy Channel Tables

Table A.1: Energy Channel Bin Characteristics from Bow Tie Analysis

Channel Number	Deposited Energy Range(MeV)	E_{nom} (MeV)	Bin Width (MeV)	Energy Resolution (%)
1	0.10 - 0.22	1.0545	0.3593	34.08
2	0.22 - 0.50	1.0939	0.2399	21.93
3	0.50 - 0.53	1.1823	0.1486	12.57
4	0.53 - 0.56	1.1997	0.1289	10.74
5	0.56 - 0.59	1.2149	0.1232	10.14
6	0.59 - 0.63	1.2457	0.1207	9.69
7	0.63 - 0.67	1.2699	0.1152	9.07
8	0.67 - 0.71	1.3062	0.109	8.35
9	0.71 - 0.75	1.3361	0.1067	7.99
10	0.75 - 0.79	1.377	0.0958	6.96
11	0.79 - 0.84	1.4218	0.1043	7.34
12	0.84 - 0.89	1.4632	0.1068	7.3
13	0.89 - 0.94	1.5083	0.107	7.1
14	0.94 - 1.00	1.5599	0.1026	6.58
15	1.00 - 1.06	1.6116	0.1095	6.79
16	1.06 - 1.12	1.6695	0.1077	6.45
17	1.12 - 1.19	1.7268	0.1151	6.66
18	1.19 - 1.26	1.7934	0.1105	6.16
19	1.26 - 1.33	1.8638	0.1238	6.64
20	1.33 - 1.41	1.9292	0.1193	6.18
21	1.41 - 1.49	2.0088	0.1181	5.88
22	1.49 - 1.58	2.0877	0.1302	6.24
23	1.58 - 1.67	2.1787	0.1293	5.94
24	1.67 - 1.77	2.272	0.1321	5.81
25	1.77 - 1.88	2.3716	0.1425	6.01
26	1.88 - 1.99	2.482	0.1415	5.7
27	1.99 - 2.10	2.5942	0.1506	5.81
28	2.10 - 2.23	2.7155	0.1562	5.75
29	2.23 - 2.36	2.8468	0.1608	5.65
30	2.36 - 2.50	2.9823	0.169	5.67
31	2.50 - 2.77	3.1846	0.2903	9.12
32	2.77 - 3.07	3.4744	0.3183	9.16
33	3.07 - 3.40	3.7992	0.3498	9.21
34	3.40 - 3.77	4.1528	0.3937	9.48
35	3.77 - 4.18	4.5493	0.4371	9.61
36	4.18 - 4.64	4.9784	0.4886	9.81
37	4.64 - 5.14	5.4488	0.5441	9.98
38	5.14 - 5.70	5.9551	0.6261	10.51
39	5.70 - 6.32	6.5068	0.7046	10.83
40	6.32 - 7.00	7.0965	0.7984	11.25

Note: Results shown are from Bow Tie analysis. The nominal incident energy range for each channel can be found by $E_{nom} \pm$ Bin Width.

Table A.2: Estimated Count Rates for each energy channel at L=4 for 25th, 50th, and 75th Percentile Fluxes from AE9

Channel Number	Deposited Energy Range(MeV)	Estimated Count Rates (count/sec) at L=4		
		25th Percentile	50th Percentile	75th Percentile
1	0.10 - 0.22	574.09	2292.39	6872.12
2	0.22 - 0.50	1356.85	5542.47	16913.53
3	0.50 - 0.53	128.59	542.45	1696.29
4	0.53 - 0.56	132.1	561.43	1765.29
5	0.56 - 0.59	141.94	607.94	1922.4
6	0.59 - 0.63	137.98	594.56	1888.7
7	0.63 - 0.67	144.96	626.8	1996.58
8	0.67 - 0.71	145.76	632.44	2020.38
9	0.71 - 0.75	148.61	647.35	2074.73
10	0.75 - 0.79	149.04	652.61	2100.57
11	0.79 - 0.84	138.38	609.95	1973.76
12	0.84 - 0.89	136.24	604.94	1969.03
13	0.89 - 0.94	130.44	584.49	1916.3
14	0.94 - 1.00	122.87	557.31	1844.46
15	1.00 - 1.06	113.19	521.32	1745.56
16	1.06 - 1.12	99.69	467.78	1588.07
17	1.12 - 1.19	91.19	433.88	1488.11
18	1.19 - 1.26	84.39	404.15	1393.58
19	1.26 - 1.33	77.9	375.71	1303.14
20	1.33 - 1.41	69.24	337.05	1177.87
21	1.41 - 1.49	58.01	286.6	1013.39
22	1.49 - 1.58	46.93	237.02	852.54
23	1.58 - 1.67	36.03	187.67	690.8
24	1.67 - 1.77	30.5	161.72	603.32
25	1.77 - 1.88	26.02	139.36	524.39
26	1.88 - 1.99	20.49	111.62	425.91
27	1.99 - 2.10	15.17	85.06	332.04
28	2.10 - 2.23	10.79	62.88	252.69
29	2.23 - 2.36	8.8	52.26	213.2
30	2.36 - 2.50	6.95	42.2	175.34
31	2.50 - 2.77	8.02	51.17	220.97
32	2.77 - 3.07	4.98	33.4	150.11
33	3.07 - 3.40	2.74	19.55	91.99
34	3.40 - 3.77	1.52	11.26	54.54
35	3.77 - 4.18	0.82	6.2	30.5
36	4.18 - 4.64	0.44	3.26	15.86
37	4.64 - 5.14	0.24	1.69	8
38	5.14 - 5.70	0.12	0.87	4.17
39	5.70 - 6.32	0.05	0.42	2.1
40	6.32 - 7.00	0.02	0.17	0.88

Note: Results shown are from using the integral method presented in Eq. 4.5. The flux profile was taken from the AE9 model for the listed location and percentiles shown.

Table A.3: Estimated Count Rates for each energy channel at L=6.6 for 25th, 50th, and 75th Percentile Fluxes from AE9

Channel Number	Deposited Energy Range	Estimated Count Rates(count/sec) at L=6.6		
		25th Percentile	50th Percentile	75th Percentile
1	0.10 - 0.22	132.84	422.66	1062.95
2	0.22 - 0.50	255.2	862.17	2271.08
3	0.50 - 0.53	19.12	69.66	194.51
4	0.53 - 0.56	18.48	68.78	195.07
5	0.56 - 0.59	18.62	70.99	204.68
6	0.59 - 0.63	17.36	67.29	196.26
7	0.63 - 0.67	18.02	70.23	205.72
8	0.67 - 0.71	18.02	70.49	207.08
9	0.71 - 0.75	18.25	71.69	211.35
10	0.75 - 0.79	18.16	71.71	212.34
11	0.79 - 0.84	16.69	66.36	197.62
12	0.84 - 0.89	16.24	65.07	195.02
13	0.89 - 0.94	15.31	61.98	187.29
14	0.94 - 1.00	14.14	58	177.17
15	1.00 - 1.06	12.69	53	164.16
16	1.06 - 1.12	10.83	46.27	145.77
17	1.12 - 1.19	9.7	42.16	134.47
18	1.19 - 1.26	8.96	39.21	125.68
19	1.26 - 1.33	8.29	36.47	117.47
20	1.33 - 1.41	7.38	32.74	106.12
21	1.41 - 1.49	6.21	27.87	91.22
22	1.49 - 1.58	5.05	23.09	76.64
23	1.58 - 1.67	3.92	18.33	61.99
24	1.67 - 1.77	3.35	15.85	54.06
25	1.77 - 1.88	2.88	13.71	46.93
26	1.88 - 1.99	2.31	11.06	38.03
27	1.99 - 2.10	1.76	8.52	29.54
28	2.10 - 2.23	1.3	6.37	22.33
29	2.23 - 2.36	1.07	5.3	18.67
30	2.36 - 2.50	0.86	4.27	15.15
31	2.50 - 2.77	1.02	5.17	18.56
32	2.77 - 3.07	0.67	3.41	12.27
33	3.07 - 3.40	0.42	2.1	7.47
34	3.40 - 3.77	0.28	1.37	4.78
35	3.77 - 4.18	0.17	0.83	2.88
36	4.18 - 4.64	0.09	0.46	1.65
37	4.64 - 5.14	0.05	0.25	0.95
38	5.14 - 5.70	0.02	0.14	0.57
39	5.70 - 6.32	0.01	0.07	0.31
40	6.32 - 7.00	0	0.02	0.07

Note: Results shown are from using the integral method presented in Eq. 4.5. The flux profile was taken from the AE9 model for the listed location and percentiles shown.

Table A.4: Energy Channel Bin Characteristics for Inner Configurations Testing

Channel Number	Deposited Energy Range	Ei (MeV)	FWHM (MeV)	Energy Resolution
1	0.10 - 0.22	1.022	0.38	37.26
2	0.22 - 0.50	1.0614	0.23	21.70
3	0.50 - 0.53	1.1508	0.13	11.34
4	0.53 - 0.56	1.1792	0.14	12.00
5	0.56 - 0.59	1.1903	0.12	10.12
6	0.59 - 0.63	1.2129	0.12	10.26
7	0.63 - 0.67	1.239	0.11	9.08
8	0.67 - 0.71	1.2724	0.11	8.82
9	0.71 - 0.75	1.3028	0.11	8.19
10	0.75 - 0.79	1.3402	0.10	7.50
11	0.79 - 0.84	1.3779	0.11	7.84
12	0.84 - 0.89	1.4186	0.10	6.75
13	0.89 - 0.94	1.4628	0.10	6.80
14	0.94 - 1.00	1.512	0.10	6.87
15	1.00 - 1.06	1.5663	0.10	6.63
16	1.06 - 1.12	1.6215	0.10	6.44
17	1.12 - 1.19	1.6803	0.11	6.80
18	1.19 - 1.26	1.7445	0.11	6.41
19	1.26 - 1.33	1.812	0.11	6.23
20	1.33 - 1.41	1.8845	0.12	6.35
21	1.41 - 1.49	1.9604	0.12	6.02
22	1.49 - 1.58	2.0428	0.12	6.02
23	1.58 - 1.67	2.1321	0.13	5.95
24	1.67 - 1.77	2.2264	0.13	5.92
25	1.77 - 1.88	2.3281	0.14	5.96
26	1.88 - 1.99	2.4357	0.14	5.94
27	1.99 - 2.10	2.5483	0.15	5.70
28	2.10 - 2.23	2.6705	0.15	5.64
29	2.23 - 2.36	2.7988	0.16	5.59
30	2.36 - 2.50	2.9355	0.16	5.55
31	2.50 - 2.77	3.1355	0.28	8.98
32	2.77 - 3.07	3.4229	0.32	9.23
33	3.07 - 3.40	3.7412	0.35	9.29
34	3.40 - 3.77	4.0939	0.39	9.59
35	3.77 - 4.18	4.4802	0.43	9.67
36	4.18 - 4.64	4.909	0.48	9.82
37	4.64 - 5.14	5.3823	0.54	10.05
38	5.14 - 5.70	5.8912	0.60	10.13
39	5.70 - 6.32	6.4572	0.67	10.43
40	6.32 - 7.00	7.0667	0.73	10.36

Table A.5: Estimated Count Rates for each energy channel for the Inner vs Whole Testing from Bow Tie Analysis at L=4 for 25th, 50th, and 75th Percentile Fluxes from AE9

Channel Number	**Deposited Energy Range(MeV)**	**Estimated Count Rates(count/sec) at L = 4**					
		Inner Configuration			**Whole Configuration**		
		25th	**50th**	**75th**	**25th**	**50th**	**75th**
1	0.10 - 0.22	736.49	2941.75	8819.82	802.86	3230.36	9745.45
2	0.22 - 0.50	1661.32	6778.65	20665.37	1764.84	7242.15	22186.15
3	0.50 - 0.53	155.01	652.96	2039.31	163.32	690.87	2165.45
4	0.53 - 0.56	149.51	636.06	2001.1	157.68	673.48	2126.03
5	0.56 - 0.59	163.23	699.15	2210.47	171.44	736.93	2337.13
6	0.59 - 0.63	165.71	713.5	2264.71	173.87	751.2	2391.46
7	0.63 - 0.67	167.92	725.16	2307.3	175.69	761.37	2429.83
8	0.67 - 0.71	173.33	751.03	2396.33	181.53	789.38	2526.44
9	0.71 - 0.75	169.85	738.78	2364.63	177.32	774.04	2485.23
10	0.75 - 0.79	167.8	733.41	2356.8	175.78	771.36	2487.26
11	0.79 - 0.84	162.36	713.83	2304.91	170.1	750.94	2433.17
12	0.84 - 0.89	158.53	702.01	2279.71	166.08	738.49	2406.64
13	0.89 - 0.94	150.88	674.24	2205.37	158.36	710.68	2332.94
14	0.94 - 1.00	137.57	622.17	2054.04	144.99	658.41	2181.32
15	1.00 - 1.06	124.06	569.97	1904.39	131.22	605.21	2028.79
16	1.06 - 1.12	109.15	510.78	1730.08	116.6	547.58	1860.31
17	1.12 - 1.19	98.37	467.05	1598.99	105.57	502.84	1726.34
18	1.19 - 1.26	91.27	436.07	1500.47	98.63	472.83	1631.83
19	1.26 - 1.33	82.47	396.69	1372.62	89.67	432.89	1502.63
20	1.33 - 1.41	70.78	343.79	1199.02	77.72	379	1326.37
21	1.41 - 1.49	59.89	294.92	1040.06	66.34	328.05	1160.97
22	1.49 - 1.58	46.83	235.78	845.83	52.75	266.63	959.78
23	1.58 - 1.67	35.06	182.11	668.72	40.24	209.73	772.51
24	1.67 - 1.77	29	153.33	570.74	33.77	179.19	668.96
25	1.77 - 1.88	24.14	128.99	484.32	28.55	153.11	576.73
26	1.88 - 1.99	18.65	101.31	385.55	22.55	122.95	469.5
27	1.99 - 2.10	13.4	74.84	291.21	16.71	93.71	365.93
28	2.10 - 2.23	9.21	53.48	214.32	11.84	69.02	277.46
29	2.23 - 2.36	7.26	42.94	174.69	9.62	57.16	233.27
30	2.36 - 2.50	5.55	33.59	139.13	7.56	45.86	190.53
31	2.50 - 2.77	6.08	38.68	166.58	8.72	55.65	240.32
32	2.77 - 3.07	3.51	23.5	105.35	5.39	36.18	162.54
33	3.07 - 3.40	1.81	12.85	60.35	2.98	21.24	99.92
34	3.40 - 3.77	0.92	6.81	32.97	1.63	12.09	58.56
35	3.77 - 4.18	0.45	3.42	16.84	0.87	6.59	32.42
36	4.18 - 4.64	0.22	1.66	8.06	0.47	3.5	17.03
37	4.64 - 5.14	0.1	0.75	3.52	0.25	1.76	8.33
38	5.14 - 5.70	0.05	0.35	1.68	0.13	0.92	4.39
39	5.70 - 6.32	0.02	0.15	0.74	0.06	0.43	2.18
40	6.32 - 7.00	0.01	0.05	0.27	0.02	0.17	0.93

Table A.6: Estimated Count Rates for each energy channel for the Inner Vs. Whole Testing from Bow Tie Analysis at L=6.6 for 25th, 50th, and 75th Percentile Fluxes from AE9

Channel Number	**Deposited Energy Range(MeV)**	**Estimated Count Rates(count/sec) at L=6.6**					
		Inner Configuration			**Whole Configuration**		
		25th	**50th**	**75th**	**25th**	**50th**	**75th**
1	0.10 - 0.22	169.38	539.73	1358.88	178.57	574.42	1458.7
2	0.22 - 0.50	312.74	1056.17	2780.33	325.43	1106.82	2932.16
3	0.50 - 0.53	23.13	84.12	234.56	24.09	88.09	246.71
4	0.53 - 0.56	20.63	77.16	219.5	21.58	81.06	231.48
5	0.56 - 0.59	21.26	81.22	234.5	22.19	85.12	246.56
6	0.59 - 0.63	20.78	80.6	235.1	21.71	84.48	247.12
7	0.63 - 0.67	20.89	81.35	238.06	21.77	85.04	249.58
8	0.67 - 0.71	21.45	83.82	245.98	22.37	87.71	258.17
9	0.71 - 0.75	20.89	81.96	241.31	21.72	85.5	252.5
10	0.75 - 0.79	20.48	80.75	238.75	21.36	84.54	250.78
11	0.79 - 0.84	19.63	77.86	231.41	20.48	81.54	243.17
12	0.84 - 0.89	18.95	75.72	226.46	19.77	79.32	238.02
13	0.89 - 0.94	17.76	71.69	216.13	18.57	75.26	227.7
14	0.94 - 1.00	15.87	64.93	197.86	16.67	68.48	209.38
15	1.00 - 1.06	13.93	58.05	179.43	14.7	61.5	190.67
16	1.06 - 1.12	11.86	50.58	159.02	12.67	54.18	170.77
17	1.12 - 1.19	10.45	45.38	144.55	11.23	48.87	156
18	1.19 - 1.26	9.68	42.29	135.35	10.48	45.87	147.15
19	1.26 - 1.33	8.76	38.49	123.77	9.54	42.02	135.44
20	1.33 - 1.41	7.54	33.38	108.05	8.29	36.82	119.48
21	1.41 - 1.49	6.4	28.66	93.65	7.1	31.9	104.49
22	1.49 - 1.58	5.03	22.95	76.07	5.68	25.98	86.27
23	1.58 - 1.67	3.8	17.78	60.04	4.38	20.49	69.31
24	1.67 - 1.77	3.17	15.01	51.18	3.71	17.57	59.94
25	1.77 - 1.88	2.67	12.68	43.37	3.17	15.07	51.6
26	1.88 - 1.99	2.1	10.03	34.46	2.54	12.18	41.91
27	1.99 - 2.10	1.55	7.48	25.94	1.94	9.38	32.54
28	2.10 - 2.23	1.11	5.41	18.96	1.43	6.99	24.51
29	2.23 - 2.36	0.88	4.35	15.32	1.17	5.79	20.42
30	2.36 - 2.50	0.68	3.4	12.04	0.93	4.64	16.46
31	2.50 - 2.77	0.77	3.9	14	1.11	5.63	20.18
32	2.77 - 3.07	0.47	2.39	8.6	0.73	3.69	13.28
33	3.07 - 3.40	0.27	1.37	4.88	0.46	2.28	8.11
34	3.40 - 3.77	0.17	0.82	2.87	0.3	1.47	5.14
35	3.77 - 4.18	0.09	0.46	1.58	0.18	0.88	3.07
36	4.18 - 4.64	0.05	0.24	0.84	0.1	0.5	1.79
37	4.64 - 5.14	0.02	0.11	0.42	0.05	0.26	1.01
38	5.14 - 5.70	0.01	0.06	0.24	0.03	0.15	0.64
39	5.70 - 6.32	0	0.03	0.12	0.01	0.08	0.37
40	6.32 - 7.00	0	0.01	0.05	0	0.04	0.17